Dalton Transactions

ROYAL SOCIETY OF CHEMISTRY

PAPER

View Article Online
View Journal

Cite this: DOI: 10.1039/d6dt00513f

Chemical synthesis of Zr-/Ce-/Sm-containing intermetallic compounds catalyzing $NaBH_4$-assisted hydrogenation of 4-nitrophenol

Yasukazu Kobayashi, *[a] Hiroshi Mizoguchi,[b] Koharu Yamamoto[c] and Ryo Shoji [c]

Received 2nd March 2026,
Accepted 13th April 2026

DOI: 10.1039/d6dt00513f

rsc.li/dalton

Zr-/Ce-/Sm-containing intermetallic compounds, specifically $ZrZnNi_4$, $CeNi_5$, $CeAlNi_4$, $CeNi_4Si$, $Ce(NiSi)_2$, $SmNi_3$, $SmNi_4Si$, and $Sm(NiSi)_2$, were synthesized by reducing the metal oxides using a CaH_2 reducing agent within molten LiCl. The resultant nanopowders exhibited high specific surface areas: $ZrZnNi_4$ (42.0 $m^2\ g^{-1}$), $CeAlNi_4$ (66.9 $m^2\ g^{-1}$), and $Sm(NiSi)_2$ (25.0 $m^2\ g^{-1}$). They were subsequently tested for their effectiveness in the $NaBH_4$-assisted hydrogenation of 4-nitrophenol. When compared to the prepared catalysts, including a conventional CeO_2-supported Ni catalyst, $ZrZnNi_4$ demonstrated the highest catalytic activity. Based on experimental results and density functional theory calculations, it was proposed that enhanced performance could be attributed to the formation of electron-rich Ni species in $ZrZnNi_4$.

Introduction

Nitrophenols are commonly utilized in various industrial applications, such as dyes, pesticides, herbicides, and pharmaceuticals. However, nitrophenols and their derivatives are toxic and present significant risks to both ecosystems and human health with prolonged exposure.[1,2] The conversion of nitrophenols into less harmful aminophenols *via* heterogeneous catalysts is a well-established method for degradation. The reduction of 4-nitrophenol (4NP) to 4-aminophenol (4AP) using $NaBH_4$ as a reducing agent has attracted considerable interest as a model reaction for assessing catalytic activity.[3] The proposed reaction mechanism follows the Langmuir–Hinshelwood model,[4] commencing with the hydrolysis of $NaBH_4$, generating $B(OH)_4^-$ and H_2 gas or reactive hydrogen (H) adsorbed on the metal surface (M) as represented in eqn (1)–(6).[5]

$$NaBH_4(S) \rightarrow Na^+ + BH_4^- \quad (1)$$

$$2M + BH_4^- \leftrightarrow M\text{–}BH_3^- + M\text{–}H \quad (2)$$

$$M\text{–}BH_3^- \leftrightarrow BH_3 + M^- \quad (3)$$

$$BH_3 + OH^- \rightarrow BH_3(OH)^- \quad (4)$$

$$M^- + H_2O \rightarrow M\text{–}H + OH^- \quad (5)$$

$$M\text{–}H + M\text{–}H \rightarrow 2M + H_2(g) \quad (6)$$

The product $BH_3(OH)^-$ generated in eqn (4) is thought to exhibit reactivity similar to that of BH_4^- and undergoes reaction steps akin to eqn (2)–(4), leading to the formation of $BH_2(OH)_2^-$. This species can engage in further reactions resulting in $BH(OH)_3^-$ and, ultimately, $B(OH)_4^-$. In the second step, the adsorbed reactive hydrogen reacts with the 4NP that is adsorbed onto the metal surface to produce 4AP, as depicted in eqn (7)–(9) through a direct pathway.[6]

$$M + 4NP \rightarrow M\text{–}4NP \quad (7)$$

$$6M\text{–}H + M\text{–}4NP \rightarrow M\text{–}4AP + 2H_2O \quad (8)$$

$$M\text{–}4AP \rightarrow M + 4AP \quad (9)$$

The rate-determining step in this process is the surface reduction of adsorbed 4NP to adsorbed 4AP (eqn (8)).[4] Consequently, it is crucial to utilize catalysts that facilitate the hydrogenation of 4NP to 4AP (eqn (8)) to enhance the overall efficiency of the process.

Precious metal nanoparticles, such as Au and Ag, are recognized for their high catalytic performance in $NaBH_4$-assisted hydrogenation.[7,8] However, low-cost catalysts comprising Ni, Co, and Fe have also been developed to reduce catalyst expenses.[9,10] To enhance the activity of these economical metal catalysts, the incorporation of other metals into the catalyst structure has been investigated.[11] Low work function (WF) metals, such as W (4.55 eV), Cr (4.5 eV), and Mn (4.1 eV),[12] have the ability to readily donate electrons to higher WF metals, such as Ni (5.15 eV) and Co (5.0 eV), as long as there is

[a]*Renewable Energy Research Center, National Institute of Advanced Industrial Science and Technology, 2-2-9 Machiikedai, Koriyama, Fukushima 963-0298, Japan. E-mail: yasu-kobayashi@aist.go.jp*
[b]*Research Center for Materials Nanoarchitectonics (MANA), National Institute for Materials Science (NIMS) Tsukuba, Ibaraki 305-0044, Japan*
[c]*Department of Chemical Science and Engineering, National Institute of Technology, Tokyo College, 1220-2 Kunugida, Hachioji, Tokyo 193-0997, Japan*

tight contact between the two, leading to the creation of electron-rich Ni and Co species. Since the rate-determining step (eqn (8)) can be accelerated by increasing the surface concentration of reactive hydrogens (H) generated on these electron-rich metals (eqn (5)), designing improved catalysts that contain electron-rich active metals is a strategic approach in the $NaBH_4$-assisted hydrogenation of 4NP.

In this study, we developed Ni-based intermetallic compound catalysts featuring very low WF metals like Zr (4.05 eV), Ce (2.9 eV), and Sm (2.7 eV).[12] The oxidation of these metals to form oxides poses a significant challenge in the preparation of alloy catalysts with nanoscale morphologies, which are essential for achieving high surface areas. This issue was addressed by employing a CaH_2-assisted molten salt synthesis method, allowing for the reduction of metals by CaH_2 to occur in an oxygen-free molten LiCl environment,[13] thus preventing oxidation. The versatility of this synthesis method was confirmed by the successful production of $ZrZnNi_4$, $CeNi_5$, $CeAlNi_4$, $CeNi_4Si$, $Ce(NiSi)_2$, $SmNi_3$, $SmNi_4Si$, and $Sm(NiSi)_2$ from the respective metal oxide precursors. The catalysts $ZrZnNi_4$, $CeAlNi_4$, and $Sm(NiSi)_2$, which possess high surface areas, were then evaluated in the context of the $NaBH_4$-assisted hydrogenation of 4NP.

Experimental

Preparation of intermetallic compound nanopowders

Zr-/Ce-/Sm-containing intermetallic compounds were synthesized by reducing metal oxides with CaH_2 as a reducing agent in molten LiCl at 600 °C. Initially, metal oxide precursors were prepared using the following citric acid method. For $ZrZnNi_4$, $CeNi_5$, $CeAlNi_4$, and $SmNi_3$, metal nitrate salts such as $ZrO(NO_3)_2{\cdot}2H_2O$ (97.0%, Wako Pure Chem. Corp.), $Zn(NO_3)_2{\cdot}6H_2O$ (99.9%, Wako Pure Chem. Corp.), $Ni(NO_3)_2{\cdot}6H_2O$ (98.0%, Wako Pure Chem. Corp.), $Ce(NO_3)_3{\cdot}6H_2O$ (98.0%, Wako Pure Chem. Corp.), $Al(NO_3)_3{\cdot}9H_2O$ (98.0%, Wako Pure Chem. Corp.), $Sm(NO_3)_3{\cdot}6H_2O$ (99.5%, Wako Pure Chem. Corp.) were dissolved in distilled water to obtain the stoichiometric molar ratios of $ZrZnNi_4$, $CeNi_5$, $CeAlNi_4$, and $SmNi_3$. For $CeNi_4Si$, $Ce(SiNi)_2$, $SmNi_4Si$, and $Sm(NiSi)_2$, the aforementioned metal nitrate salts were dissolved in distilled water and mixed with SiO_2 nanoparticles (99.5%, 10–20 nm, Sigma-Aldrich Co. LLC.) to achieve the stoichiometric ratios necessary for $CeNi_4Si$, $Ce(NiSi)_2$, $SmNi_4Si$, and $Sm(NiSi)_2$. Subsequently, citric acid was incorporated into the solutions at a molar ratio of total metals/citric acid = 1/1.2. After thorough mixing, the resultant solution was evaporated on a hot plate at 110 °C overnight. The resulting dried powder was initially heated in air at 250 °C for 2 hours and then gently ground in a mortar to create a homogeneous powder. Lastly, the powder was heated in air at 500 °C for 2 hours to produce the metal oxide precursors.

Next, the metal oxide precursor, CaH_2 (94.0%, JUNSEI Chem. Co.), and LiCl (99.0%, Wako Pure Chem. Corp.) were blended in a mortar in a weight ratio of 2/6/3 of metal oxide precursor/CaH_2/LiCl. This mixed powder was placed in a stainless-steel container filled with Ar gas and heated at 600 °C for 2 hours. The reduced precursors were then crushed in a mortar and rinsed multiple times with a 0.4 M NH_4Cl aqueous solution, followed by distilled water. The final dried products were designated as $ZrZnNi_4$, $CeNi_5$, $CeAlNi_4$, $CeNi_4Si$, $Ce(NiSi)_2$, $SmNi_3$, $SmNi_4Si$, and $Sm(NiSi)_2$.

The $ZrNi_5$ ingot for WFs measurement was prepared by arc melting a stoichiometric mixture of Zr and Ni elements on a water-cooled Cu hearth under a high-purity argon atmosphere. Annealing was subsequently conducted at 1000 °C for 20 hours to produce the single phase.

Characterization of intermetallic compound nanopowders

The crystal structure was analyzed utilizing X-ray diffraction (XRD; SmartLab, 3 kW, Rigaku Corporation) with CuK_α radiation at 40 kV and 30 mA. Porosity was assessed through N_2 adsorption and desorption at −196 °C (BELLSORP mini-II, Microtrac-BEL). The pore size distribution was derived from the measured adsorption isotherms using the Barrett, Joyner, and Halenda (BJH) method for all samples. Prior to measurement, the samples were pretreated at 150 °C for 60 minutes under vacuum. Scanning electron microscopy (SEM; JSM-7400F, JEOL Ltd) was employed to observe the morphology, with energy dispersive X-ray spectrometry (EDX) utilized for elemental analysis. X-ray fluorescence (XRF; ZSX PrimusII, 3 kW, Rigaku Corporation) was conducted in air to detect elements within the samples, except for lighter elements such as H, He, Li, N, and O. The chemical states and surface composition of the prepared sample were analyzed using X-ray photoelectron spectroscopy (XPS; PHI X-tool, ULVAC-PHI), operated with AlK_α radiation. The chemical shifts were calibrated by fixing the C1s peak of surface carbonaceous contaminants at 284.5 eV. Photoemission yield spectra were recorded in air to estimate the WFs using a RIKENKEIKI AC-2 spectrometer, which collected photoelectrons emitted from the polished surface of $ZrNi_5$ ingots upon UV light excitation through O_2 molecule mediation.

Catalytic test with intermetallic compound nanopowders

The catalytic reactions were performed in 20 mL glass bottles following previously documented protocols. In the catalytic tests, a 1 mL solution of *p*-nitrophenol (4NP) at 14 mM was combined with 10 mg of catalyst powder, 1 mL of $NaBH_4$ solution (0.42 M), and 7 mL of distilled water as the solvent. To ensure pseudo first-order reaction kinetics, the initial concentration of $NaBH_4$ (0.047 M) was set 30 times greater than that of 4NP (1.6 mM). The reactions were carried out under stirring at room temperature (25 °C) for 60 minutes. An aluminum heat sink on a hot plate was used to maintain a constant solution temperature. A small aliquot (100 μL) of the reaction solution was extracted to evaluate concentration changes throughout the reaction. The conversion of 4NP to *p*-aminophenol (4AP) was monitored using an ultraviolet-visible spectrometer (Shimadzu, UV-1280), through the corresponding absorbance changes at 401 and 315 nm.

For comparison, a 12 wt% NiO or 10 wt% Ni catalyst supported on commercial CeO_2 nanopowder (30 m^2 g^{-1}, <50 nm, Sigma-Aldrich Co. LLC) was prepared using a conventional impregnation method. Initially, $Ni(NO_3)_2{\cdot}6H_2O$ was dissolved in distilled water, and a suspension was created with CeO_2 to achieve a 12 wt% NiO loading. The resulting suspension was then evaporated on a hot plate at 110 °C overnight. The dried powder was subsequently heated in air at 500 °C for 2 hours to yield the 12 wt%NiO/CeO_2 catalyst. The metallic state nickel-loaded catalyst, denoted as 10 wt%Ni/CeO_2, was obtained after a reduction treatment of the NiO/CeO_2 catalyst at 400 °C under a H_2 flow at 100 mL min^{-1} for 2 hours.

Electronic structure calculations

Density functional theory (DFT) periodic calculations were conducted using the generalized gradient approximation and the Perdew–Burke–Ernzerhof functional[14] and, along with the projected augmented plane wave method[15] implemented in the Vienna *Ab initio* simulation package.[16] An energy cutoff of 600 eV was applied, and a gamma-centered *k*-mesh of 10 × 10 × 10 was utilized. A Wigner–Seitz radius of 0.146 nm was employed for the site projections of all atoms. Atomic charges were determined through Bader charge analysis,[17] and the crystal structures were visualized with the VESTA software.[18]

Results and discussion

Preparation of intermetallic compound nanopowders

Eight intermetallic compounds—$ZrZnNi_4$, $CeNi_5$, $CeAlNi_4$, $CeNi_4Si$, $Ce(NiSi)_2$, $SmNi_3$, $SmNi_4Si$, and $Sm(NiSi)_2$—were synthesized by reducing metal oxides with a CaH_2 reducing agent in molten LiCl. Fig. 1 and Fig. S1–S5 display the XRD patterns of the metal oxide precursors, each identified in blue above the corresponding figure. Peaks associated with NiO (PDF01-071-1179) were present in all oxide precursors. Additionally, CeO_2 (PDF03-065-5923) was also detected in the oxide precursors of $CeNi_5$, $CeNi_4Si$, and $Ce(NiSi)_2$. Other metal oxides, including ZrO_2, ZnO, SiO_2, and Sm_2O_3, were not observed, suggesting they may exist in an amorphous form. The metal oxide precursors were subsequently reduced and washed to yield intermetallic compound nanopowders. The XRD patterns of the intermetallic compounds, shown in Fig. 1 and Fig. S1–S5 are described in orange below each figure. The peaks from the metal oxide precursors were absent, while the expected peaks for the intermetallic compounds $ZrZnNi_4$, $CeNi_5$, $CeAlNi_4$, $CeNi_4Si$, $Ce(NiSi)_2$, $SmNi_3$, $SmNi_4Si$, and $Sm(NiSi)_2$ appeared in the reduced samples. The peaks assigned to the metallic Ni were not observed in the reduced samples. Impurity peaks assigned to $CaCO_3$ were observed in $CeNi_5$ and $Ce(SiNi)_2$, probably due to the incomplete removal of Ca species from the samples. The peak shift was observed in $CeNi_4Si$, indicating the formation of deformed structure probably due to the deviation of composition in the synthesized sample. These results indicate that the reduction of the metal oxide precursors using the CaH_2 reducing agent in molten LiCl effectively formed the intermetallic compounds. The identified crystal types and crystallite sizes, calculated using the Scherrer equation based on the main peaks detected at 2θ, are summarized in Table 1. The calculated sizes ranged from 12.2 to 52.5 nm, indicating the formation of nanoscale morphologies.

For representative samples, we briefly outline their crystal structure features. $CeNi_5$ adopts the $CaCu_5$-type crystal structure (hexagonal, $P6/mmm$, $Z = 1$),[19] as illustrated in Fig. 2(a). This structure consists of alternating layers of Ni_3 kagome layer (A) and a closed-packed layer of $CeNi_2$ (B), stacked along the [001] direction in an ABAB sequence. In this arrangement, the larger Ce ion is nestled between two Ni_6 hexagons of the kagome layer. Conversely, $ZrNi_5$ exhibits the $AuBe_5$-type crystal structure (cubic, $F\bar{4}3m$, $Z = 4$),[20] as presented in Fig. 2(b). In this case, Ni_3 kagome layer (A) and $ZrNi_2$ closed-packed layer (B) are stacked in an alternating fashion along the ⟨111⟩ direction, following the sequence of (AB)(AB)′(AB)″(AB)(AB)′(AB)″. Due to the smaller size of the Zr ion, the $ZrNi_2$ closed-packed layer displays a buckled structure, resulting in the formation

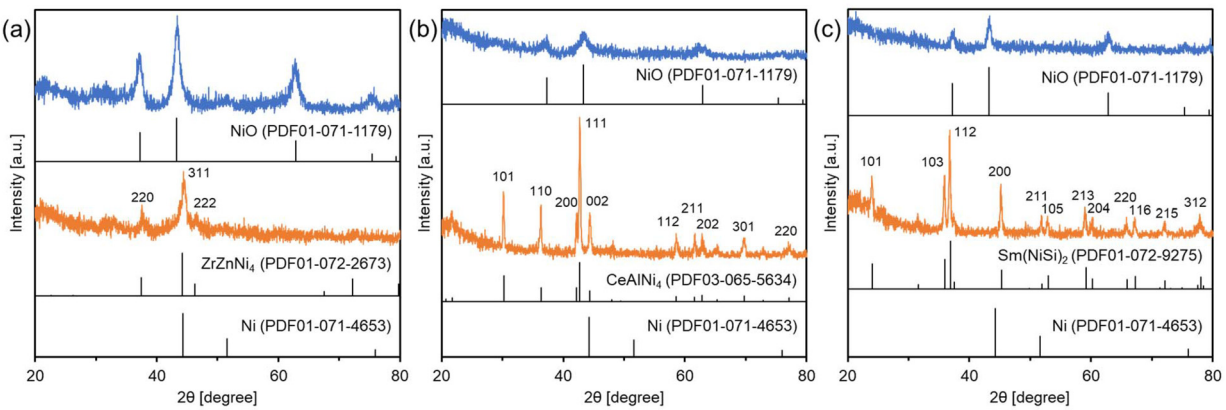

Fig. 1 XRD patterns for the oxide precursors (blue) and the reduced samples (orange) of (a) $ZrZnNi_4$, (b) $CeAlNi_4$, and (c) $Sm(NiSi)_2$. The main peaks observed in the reduced samples are described with their index values.

Table 1 Summary of the measured properties, including BET surface area (SA), pore volume (V_p), crystallite size, and elemental composition. The crystallite sizes were calculated using the Scherrer equation applied to the main peaks detected at 2θ as described in the table

		Crystallinity		Porosity		Composition		
Sample	Crystal structure	Crystallite size [nm]	2θ [degree]	BET SA [m^2 g^{-1}]	V_p [cm^3 g^{-1}]	SEM-EDX [mol%]	XRF [mol%]	XPS [mol%]
$ZrZnNi_4$	$AuBe_5$	12.2	44.3	42.0	0.094	Zr/Zn/Ni = 19.7/8.1/72.2	Zr/Zn/Ni = 22.4/7.9/69.8	Zr/Zn/Ni = 48.7/19.2/32.1
$CeNi_5$	$CaCu_5$	52.5	43.3	31.3	0.131	—	—	—
$CeAlNi_4$	$CaCu_5$	49.1	42.7	66.9	0.089	Ce/Al/Ni = 17.3/26.5/56.1	Ce/Al/Ni = 18.6/14.5/66.9	Ce/Al/Ni = 5.8/47.1/47.1
$CeNi_4Si$	$DyNi_4Si$	15.7	43.9	16.7	0.099	—	—	—
$Ce(NiSi)_2$	$Th(CrSi)_2$	21.9	36.7	33.4	0.187	—	—	—
$SmNi_3$	$PuNi_3$	41.9	36.0	6.8	0.038	—	—	—
$SmNi_4Si$	$DyNi_4Si$	19.9	37.0	14.7	0.138	—	—	—
$Sm(NiSi)_2$	$Th(CrSi)_2$	45.0	45.2	25.0	0.179	Sm/Ni/Si = 19.8/36.2/44.0	Sm/Ni/Si = 24.8/44.1/31.1	Sm/Ni/Si = 24.1/6.3/69.5

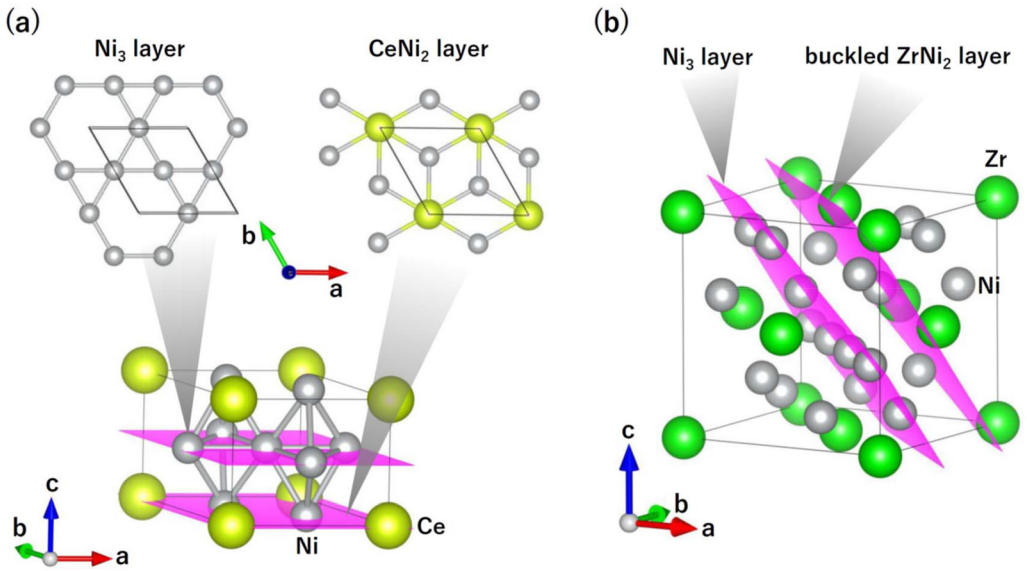

Fig. 2 (a) The crystal structure of $CeNi_5$, which includes the Ni_3 kagome layer and the $CeNi_2$ closed-packed layer, and (b) the crystal structure of $ZrNi_5$, composed of the Ni_3 kagome layer and a buckled $ZrNi_2$ closed-packed layer.

of a Frank–Kasper polyhedron around the Zr atoms. Consequently, the packing density of Ni in $ZrNi_5$ is enhanced compared to that in $CeNi_5$. The stacking arrangement observed in $ZrNi_5$ is reminiscent of the cubic Laves-type crystal structure (XY_2, $Fd\bar{3}m$, $Z = 8$),[21] where the Y_3 kagome layer (A) and X_2Y closed-packed layer (B) are also alternately stacked along the ⟨111⟩ direction in the same pattern. In $ZrNi_5$, there are two distinct crystallographic sites for Ni (4c and 16e). The formation of $Zr(ZnNi_4)$ involves substituting Ni (4c site) with Zn, leading to a 1.5% increase in the cubic lattice constant.[22]

The electronic structure of $ZrNi_5$, which serves as a parent compound to $ZrZnNi_4$, was examined using DFT calculations. Fig. 3(a) and (b) illustrate the electronic structures of $ZrNi_5$ and $ZrZnNi_4$, including the energy–wave vector (E–k) diagram and the projected density of states (DOS). The energy scale is set such that the Fermi energy (E_F) is at zero. Several energy bands intersect E_F, suggesting a metallic nature of the electronic structure. A significant DOS is observed primarily from the Ni 3d orbitals in the energy range of −3.0 to +0.3 eV. Notably, there is a pseudo bandgap around +1.9 eV, as indicated in the E–k diagram. The contribution of Zr 4d character is apparent in the unoccupied band with a narrow bandwidth around +2.5 eV. According to the Badar charge analysis, the atomic charges are estimated as $Zr^{+1.58}Ni^{-0.32}{}_5$ for $ZrNi_5$ and $Zr^{+1.60}Zn^{+0.11}Ni^{-0.43}{}_4$ for $ZrZnNi_4$. This pattern of charges aligns well with those derived from electronegativity values (Zr 1.22, Zn 1.66, Ni 1.75).[23] Negatively charged late transition metal ions, such as $Ni^{\delta-}$, typically play an important role in hydrogenation processes for hydrogen storage applications.[24] The substitution of Zn, which has a relatively positive charac-

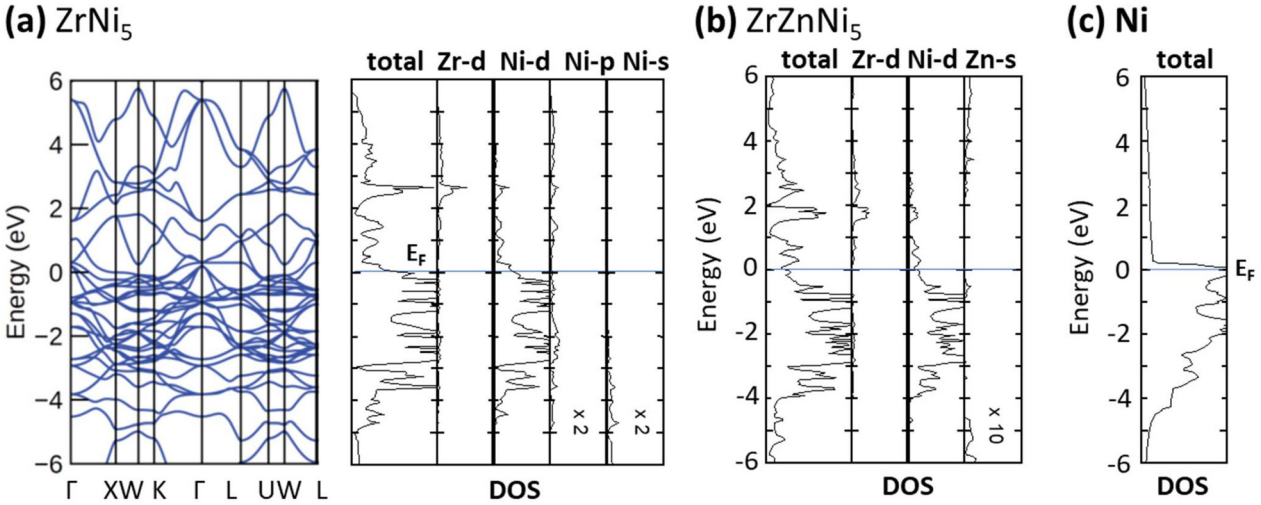

Fig. 3 (a) The calculated band structure and projected density of states for $ZrNi_5$. (b) The calculated total density of states for $ZrZnNi_4$. (c) The calculated total density of states of Ni. Magnetic ordering is not included. The calculations were performed on the primitive unit cell to reduce computational time.

ter, promotes the reduction of the remaining Ni ions, resulting in an increase in E_F energy. This shift in energy is confirmed by the unoccupied Zr 4d band, which is situated around +1.7 eV within the total DOS of $ZrZnNi_4$ (Fig. 3(b)). A subtle indication of Zn substitution can be seen in the Zn $3d^{10}$ band located approximately at −7.2 eV, which does not contribute to the electronic structure near E_F (not shown in Fig. 3(b)). Now, let's consider the changes brought about by alloying Zr with Ni. We show calculated DOS of metallic Ni in Fig. 3(c), as a reference. The addition of Zr into Ni leads to two effects. One is the redox reaction, that is, electron transfer from Zr to Ni. The energy levels of the Zr bands are pushed lower due to the oxidation of Zr, while the Ni bands are elevated because of increased electron repulsion resulting from the reduction of Ni. Consequently, the WF of $ZrNi_5$ decreases compared to that of Ni metal, since the DOS at E_F in $ZrNi_5$ is dominated by the Ni 3d bands. This prediction is supported by the measured WF value of 4.2 eV, which is considerably lower than that of Ni metal (4.9 eV). The energy shift of WF (0.7 eV) is consistent with the shift (~0.8 eV) of unoccupied Zr 4d band mentioned above. Another effect of addition of Zr is drastic decrease of DOS(E_F). Metallic Ni has large DOS(E_F), which often induces magnetic ordering, because of the (3d4s) electronic configuration. Electron-doping into Ni by Zr fills remaining unoccupied 3d band, resulting in the decrease of DOS(E_F), whereas the WF decreases. Thus, catalytic activity due to the electron of Ni 3d band has the tradeoff relation.

Subsequently, the porosity of the prepared intermetallic compound nanopowders was assessed through nitrogen adsorption/desorption experiments. Fig. 4 and Fig. S6–S10 display the nitrogen adsorption/desorption isotherms along with the corresponding pore size distributions. The measured BET surface areas and pore volumes are collated in Table 1. A distinct hysteresis in the isotherms, with pore formation occurring at 3.8 nm, was evident in $ZrZnNi_4$. A negligible hysteresis was observed in $CeAlNi_4$, also featuring pore formation at 3.8 nm. This pore creation likely contributes to the high BET surface areas of 42.0 $m^2\ g^{-1}$ for $ZrZnNi_4$ and 66.9 $m^2\ g^{-1}$ for $CeAlNi_4$. Conversely, other samples such as $CeNi_5$, $CeNi_4Si$, $Ce(NiSi)_2$, $SmNi_3$, $SmNi_4Si$, and $Sm(NiSi)_2$ did not exhibit hysteresis, indicating no small pore formation below 10 nm.

The morphologies of representative samples $ZrZnNi_4$, $CeAlNi_4$, and $Sm(NiSi)_2$, which contain Zr, Ce, and Sm, respectively, were examined *via* SEM (Fig. S11–S13). Numerous fine particles measuring less than a micrometer were distinctly visible across all samples, and the surfaces appeared to possess nanoscale structures, leading to elevated specific surface areas. Fig. 5 presents the elemental mappings for the constituent elements of $ZrZnNi_4$, $CeAlNi_4$, and $Sm(NiSi)_2$. The constituent elements appeared well-distributed among the particles, with overlapping distributions indicating a thorough mixture of the components. It is noted that the ideal spherical particles were observed in $CeAlNi_4$, which are enclosed by rectangles in Fig. 5(b). According to the elemental mappings, the core of the particles had dense concentrations of Ni, whereas Ce was distributed in the shell. Thus, the results indicated that the formation of core–shell structures.

The compositions of $ZrZnNi_4$, $CeAlNi_4$, and $Sm(NiSi)_2$ were analyzed using SEM-EDX and XRF, with the results summarized in Table 1. The spectra obtained from SEM-EDX and XRF are shown in Fig. S14 and S15–S17, respectively. In the case of $ZrZnNi_4$, the molar ratio of Zn was lower than the stoichiometric ratio expected for the $AuBe_5$-type intermetallic compound with a Ni site substituted by Zn, indicating that the Ni site was not fully occupied by a Zn atom, resulting in a partial deficiency of Zn. For $CeAlNi_4$, the molar ratio of Ni was slightly less than what would be expected for the $CaCu_5$-type intermetallic compound with an Al atom substituted for Ni, suggesting

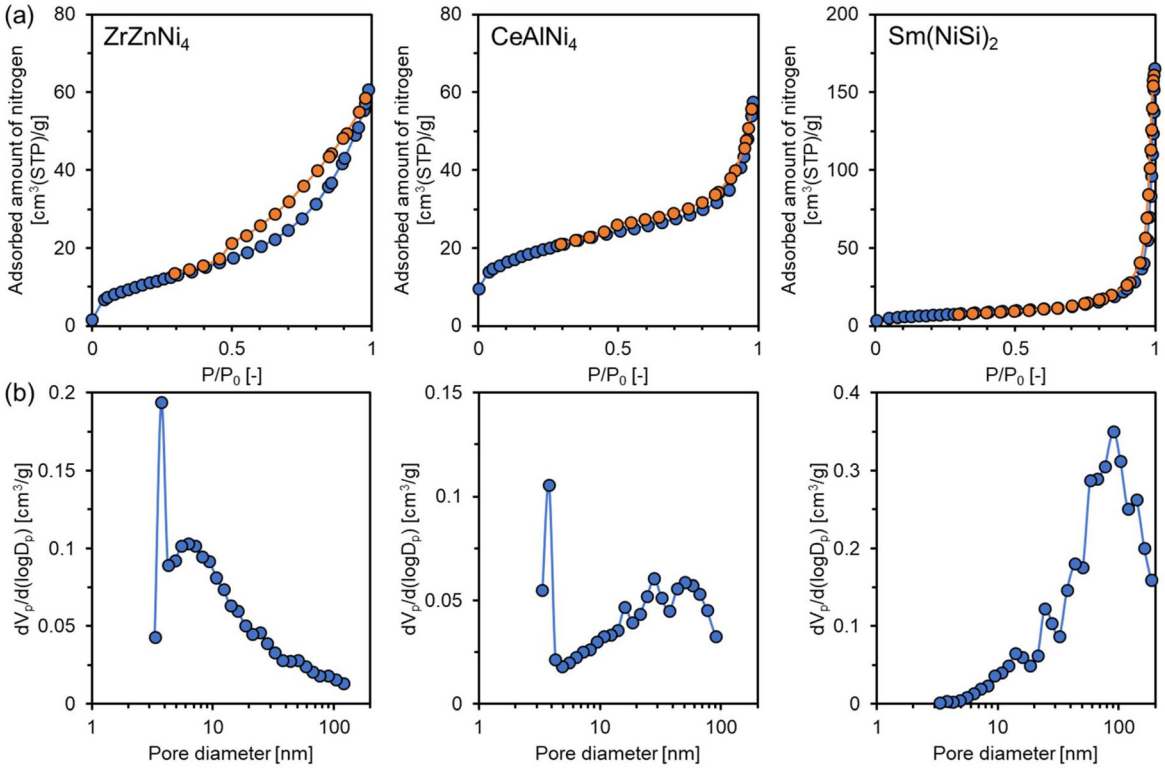

Fig. 4 (a) The adsorption (blue) and desorption (orange) isotherms of nitrogen, as well as (b) the corresponding pore size distributions for $ZrZnNi_4$, $CeAlNi_4$, and $Sm(NiSi)_2$.

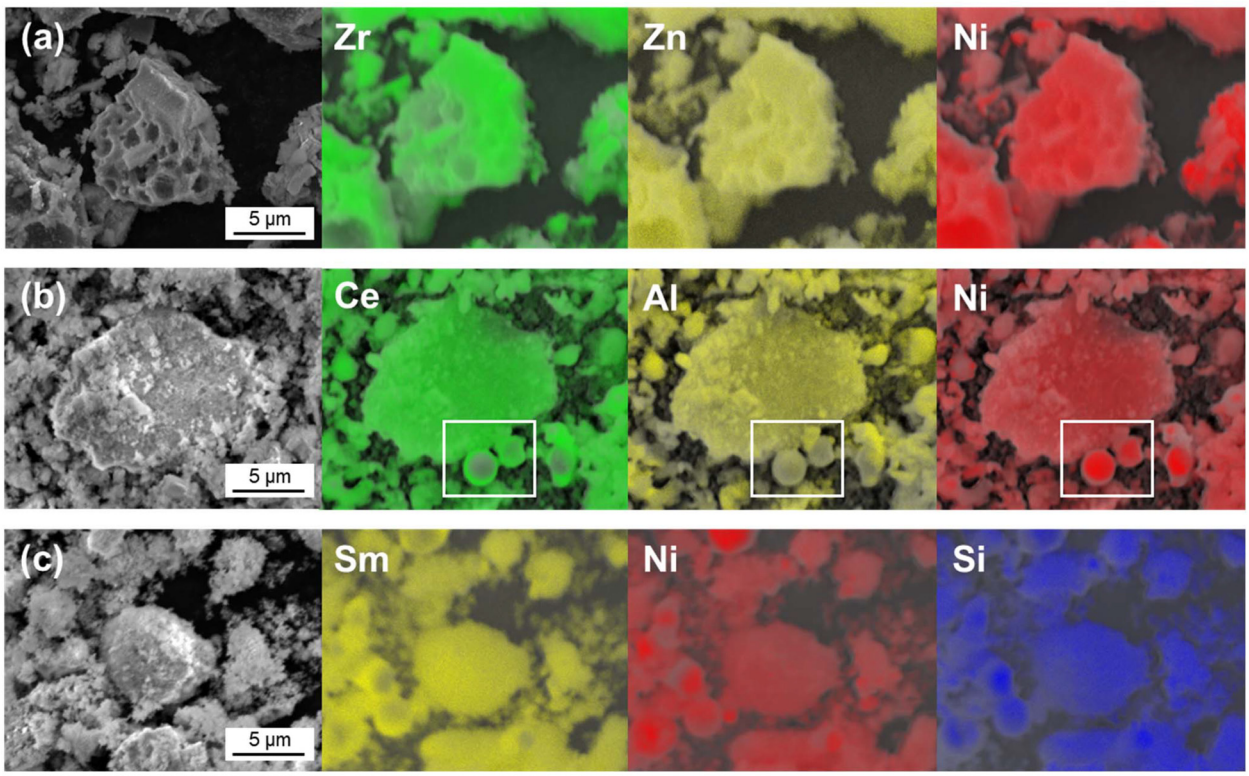

Fig. 5 SEM images and elemental mappings for (a) $ZrZnNi_4$, (b) $CeAlNi_4$, and (c) $Sm(NiSi)_2$, with corresponding EDX spectra shown in Fig. S14.

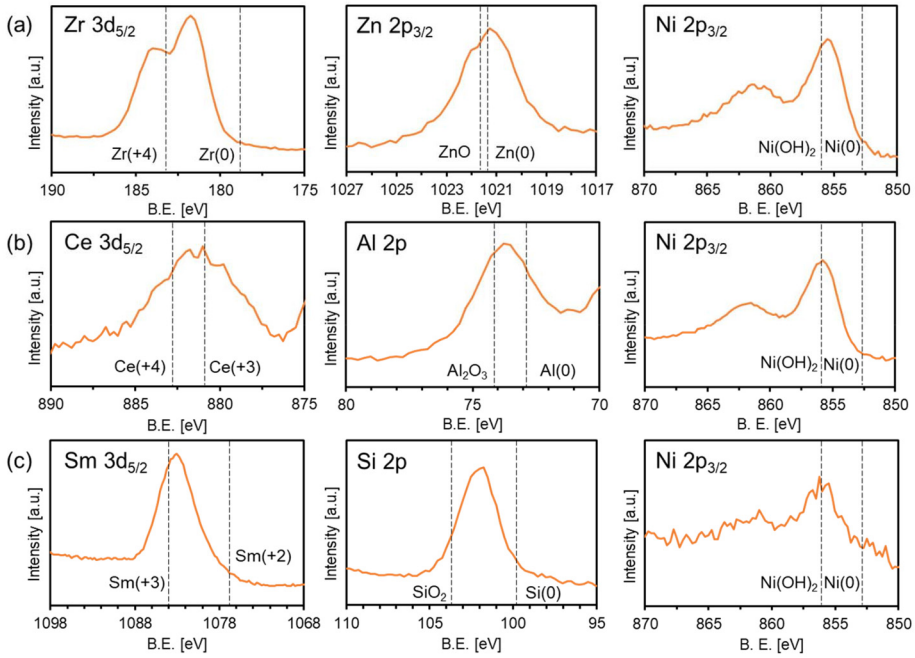

Fig. 6 XPS spectra for (a) Zr 3p5/2, Zn 2p3/2, Ni 2p3/2 for $ZrZnNi_4$, (b) Ce 3d5/2, Al 2p, Ni 2p3/2 for $CeAlNi_4$, and (c) Sm 3d5/2, Si 2p, Ni 2p3/2 for $Sm(NiSi)_2$.

a slight deficiency in Ni. For $Sm(NiSi)_2$, the molar ratio of Sm/Ni/Si was nearly in accordance with the stoichiometric ratio for the $Th(CrSi)_2$-type intermetallic compound, indicating successful synthesis of $Sm(NiSi)_2$. Detailed analysis through XRF revealed very minimal amounts of impurities in $ZrZnNi_4$, $CeAlNi_4$, and $Sm(NiSi)_2$ (Tables S1–S3). It is noteworthy that the detected amounts of Ca were minimal in all samples, suggesting that impurities originating from CaH_2, including CaH_2, CaO, $Ca(OH)_2$, and $CaCl_2$, were effectively removed through washing with a weak acid solution during the preparation process.

Catalytic performance of intermetallic compound nanopowders

The $NaBH_4$-assisted hydrogenation of 4-nitrophenol (4NP) to 4-aminophenol (4AP) follows the Langmuir–Hinshelwood model, making it crucial to examine the surface species that directly facilitate this reaction. Consequently, surface-sensitive XPS measurements were conducted on $ZrZnNi_4$, $CeAlNi_4$, and $Sm(NiSi)_2$. Fig. 6 presents the XPS spectra calibrated by aligning the C1s peak of surface carbonaceous contaminants to 284.5 eV (see Fig. S18). The resulting surface compositions are summarized in Table 1.

For $ZrZnNi_4$ shown in Fig. 6(a), a prominent peak attributed to Ni 2p3/2 was detected at 855.5 eV. Previous studies indicate that a peak associated with Ni(+2) in $Ni(OH)_2$ appears at 856.2 eV, while a peak for Ni(0) is found at 852.6 eV.[25] Hence, the oxidation state of surface nickel in $ZrZnNi_4$ is close to Ni(+2). Additionally, a peak corresponding to Zr 3d5/2 appeared at 181.5 eV. As reported earlier, peaks linked to Zr(+4) in ZrO_2 and Zr(0) can be found at 182.75 eV and 178.52 eV, respectively.[26] This suggests that the surface oxidation state of zirconium in $ZrZnNi_4$ is Zr(+4>, >0), or greater than zero. A peak corresponding to Zn 2p3/2 was observed at 1,021.1 eV. According to prior reports, Zn 2p lines are not highly sensitive to chemical environments, making it challenging to differentiate between Zn(0) (1,021.4 eV) and Zn(+2) (1,021.7 eV).[27] These findings indicate that the surface components of $ZrZnNi_4$ largely exist in higher oxidation states, such as Ni(+2) and Zr(+4>, >0). The measured surface composition of Zr/Zn/Ni = 48.7/19.2/32.1 deviated significantly from those obtained by SEM-EDX and XRF, with the molar ratio of Ni being considerably lower than the stoichiometric ratio; thus, Zr–Zn–O comprised the primary surface components. Because no oxide phases were observed in the XRD measurement (Fig. 1(a)), the thickness of the surface oxide layers could be very thin or/and the crystallinity was very low enough not to be detected by XRD.

In the case of $CeAlNi_4$, depicted in Fig. 6(b), the main peak corresponding to Ni 2p3/2 was recorded at 856.2 eV, which identifies the oxidation state of surface nickel in $CeAlNi_4$ as Ni (+2). A peak associated with Ce 3d5/2 was found at 881.3 eV. Previous studies identified peaks for Ce(+4) in CeO_2 and Ce (+3) in $CePO_4$ at 882.7 eV and 880.9 eV, respectively.[28] Therefore, the oxidation state of surface cerium in $CeAlNi_4$ approximates Ce(+3). A peak for Al 2p was detected at 73.5 eV, with prior reports indicating that peaks for Al(+3) in Al_2O_3 and Al(0) appear at 74.14 eV and 72.87 eV respectively.[29,30] Therefore, the oxidation state of surface Al in $CeAlNi_4$ is Al (+3>, >0), or greater than zero. These results indicate that the

surface compounds in $CeAlNi_4$ primarily exist in higher oxidation states, such as Ni(+2), Ce(+3), and Al(+3>, >0). The measured surface composition of Ce/Al/Ni = 5.8/47.1/47.1 showed significant deviation from SEM-EDX and XRF results, with the molar ratios of Al and Ni being considerably higher than the stoichiometric ratio; consequently, Al–Ni–O emerged as the main surface components. Because no oxide phases were observed in the XRD measurement (Fig. 1(b)), the thickness of the surface oxide layers could be very thin or/and the crystallinity was very low enough not to be detected by XRD.

For $Sm(NiSi)_2$, as shown in Fig. 6(c), a significant peak assigned to Ni 2p3/2 was noted at 856.2 eV, indicating that the oxidation state of surface Ni in $Sm(NiSi)_2$ is Ni(+2). A peak corresponding to Sm 3d5/2 appeared at 1082.8 eV. Previous reports indicate that the peaks for Sm(+3) and Sm(+2) are found at 1084.0 eV and 1076.4 eV, respectively.[31] Therefore, the oxidation state of surface Sm in $Sm(NiSi)_2$ appears to be close to Sm(+3). A peak corresponding to Si 2p was observed at 101.8 eV, with previous reports showing that peaks for Si(+4) in SiO_2 and Si(0) are found at 103.8 eV and 99.8 eV, respectively.[32] Thus, the oxidation state of surface Si in $Sm(NiSi)_2$ is Si(+4>, >0). These results point to surface compounds in $Sm(NiSi)_2$ mostly existing in higher oxidation states, such as Ni(+2), Sm(+3), and Si(+4>, >0). Additionally, the measured surface composition of Sm/Ni/Si = 24.1/6.3/69.5 significantly differed from those obtained *via* SEM-EDX and XRF. The Ni molar ratio was notably smaller than the stoichiometric ratio, and thus Sm–Si–O was determined to be the main surface component. Because no oxide phases were observed in the XRD measurement (Fig. 1(c)), the thickness of the surface oxide layers could be very thin or/and the crystallinity was very low enough not to be detected by XRD.

Next, the hydrogenation of 4-nitrophenol (4NP) to 4-aminophenol (4AP) was facilitated by $NaBH_4$ at room temperature using $ZrZnNi_4$, $CeAlNi_4$, and $Sm(NiSi)_2$. The three intermetallics were chosen as representative catalysts containing very low WF metals of Zr, Ce, and Sm, respectively, with high BET surface areas available for the catalytic reactions. 12 wt%NiO/CeO_2 and 10 wt%Ni/CeO_2 were used as a reference. XRD analysis revealed that the reference catalysts of NiO/CeO_2 and Ni/CeO_2 contained minuscule peaks of NiO and Ni, respectively, alongside significant peaks corresponding to CeO_2 (Fig. S19), indicating that small particles of NiO and Ni were successfully dispersed on CeO_2, respectively. In Fig. 7(a), the change in absorbance of the reaction mixture is plotted over time with the $ZrZnNi_4$ catalyst. The absorbance at 401 nm, associated with the concentration of 4NP, rapidly decreased over time, while the absorbance at 315 nm, which corresponds to 4AP, increased as the reaction progressed. By converting these absorbance changes into concentration variations, the plots showing concentration changes of 4NP and 4AP were obtained, as illustrated in Fig. 7(b). It was confirmed that the conversion of 4NP to 4AP occurred in a nearly stoichiometric manner. Fig. 7(c) illustrates the normalized concentration changes (C/C_0) of 4NP with $ZrZnNi_4$, $CeAlNi_4$, $Sm(NiSi)_2$, and the reference catalysts of 12 wt%NiO/CeO_2 and 10 wt%Ni/CeO_2. The concen-

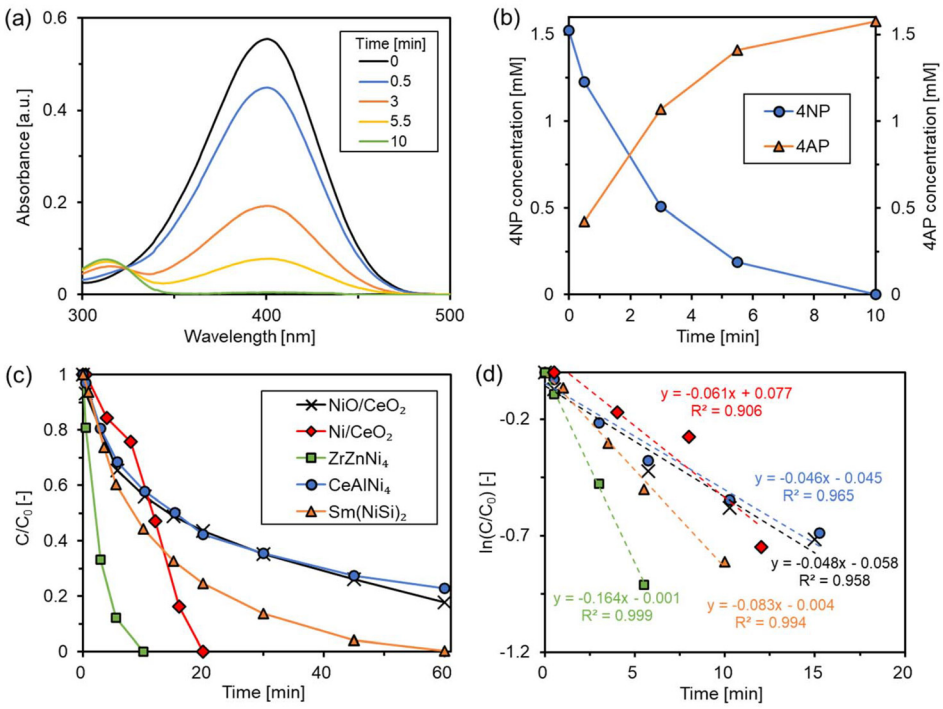

Fig. 7 (a) Changes in absorbance and (b) the concentration shifts of 4NP and 4AP over time in the reaction solution utilizing $ZrZnNi_4$ catalyst. (c) Changes in normalized concentration (C/C_0) of 4NP during the reactions and (d) the linear relationship of $\ln(C/C_0)$ over time for 12 wt%NiO/CeO_2 (X), 10 wt%Ni/CeO_2 (diamond), $ZrZnNi_4$ (square), $CeAlNi_4$ (circle), and $Sm(NiSi)_2$ (triangle) catalysts.

trations showed a gradual decrease with $CeAlNi_4$ and NiO/CeO_2, achieving nearly 80% conversion in 60 minutes. In contrast, $ZrZnNi_4$, $Sm(NiSi)_2$, and Ni/CeO_2 achieved complete conversion within 60 minutes, with $ZrZnNi_4$ reaching 100% conversion in just 10 minutes, indicating its superior catalytic activity. In comparison with NiO/CeO_2 and Ni/CeO_2, it was suggested that metallic state Ni was effective to achieve the quick complete conversion. From the plots of $\ln(C/C_0)$ against reaction time (Fig. 7(d)), the rate constants were determined as 0.16 min^{-1} for $ZrZnNi_4$, 0.04 min^{-1} for $CeAlNi_4$, 0.08 min^{-1} for $Sm(NiSi)_2$, 0.04 min^{-1} for NiO/CeO_2, and 0.06 min^{-1} for Ni/CeO_2. Comparing these constants to our previous studies conducted under the same reaction conditions but with different catalysts (Table 2), $ZrZnNi_4$ demonstrated a higher catalytic performance than the alloy catalysts CrMnFeCoNi and AlCoCrFeNi, yet lower performance than 5 wt%Pd/ZnO and $Al_{0.2}Co_{1.5}CrFeNi_{1.5}Ti_{0.5}$.

The reaction rates were observed in the following order: $ZrZnNi_4$ > $Sm(NiSi)_2$ > $CeAlNi_4$, NiO/CeO_2. XPS results indicated that a minimal quantity of Ce was present on the surface of $CeAlNi_4$, with Al–Ni–O being the primary surface component. This suggests that the active Ni species may not have effectively interacted with Ce, limiting electron transfer from Ce to Ni and thereby resulting in reduced catalytic performance for $CeAlNi_4$. Conversely, XPS analysis showed that Zr and Sm were predominantly present on the surfaces of $ZrZnNi_4$ and $Sm(NiSi)_2$, respectively, implying that active Ni species could interact effectively with Zr and Sm. This efficient electron donation from Zr and Sm to Ni likely activated the Ni species, leading to higher catalytic performance in $ZrZnNi_4$ and $Sm(NiSi)_2$. Notably, DFT calculations revealed that $ZrZnNi_4$ acts as a reductive intermetallic compound with the capability to release electrons, which aids in the generation of reactive hydrogen and accelerates the rate-determining step (eqn (8)). Although it was suggested that the synthesized $ZrZnNi_4$ had a core–shell structure that very thin oxide layers covered the intermetallic-phase core, it is possible that the electron-rich Ni species ($Ni^{\delta-}$), suggested by DFT calculations, may be partially exposed on surface through the pit-hole of the oxide shell, or/and the crystallized intermetallic $ZrZnNi_4$ existing in the core may promote the surface reaction due to the electron donation through the thin oxide shell. Therefore, the intermetallic compound $ZrZnNi_4$ stands out as a distinct catalyst, with its electron-rich Ni species effectively facilitating the $NaBH_4$-assisted hydrogenation of 4NP.

Table 2 The comparison of rate constants (k) for the hydrogenation of 4NP

Catalyst	Conditions	k [min^{-1}]	Ref.
$ZrZnNi_4$	25 °C; 4-NP (1.6 mM);	0.16	This
$CeAlNi_4$	$NaBH_4$ (47 mM); 10 mg-cat/9 mL	0.04	work
$Sm(NiSi)_2$		0.08	
12 wt%NiO/CeO_2		0.04	
10 wt%Ni/CeO_2		0.06	
5 wt%Pd/ZnO		0.44	33
$Al_{0.2}Co_{1.5}CrFeNi_{1.5}Ti_{0.5}$		0.29	34
CrMnFeCoNi		0.11	35
AlCoCrFeNi		0.03	36

Conclusions

Eight intermetallic compounds containing Zr, Ce, or Sm were synthesized through the reduction of metal oxides. The catalysts $ZrZnNi_4$ (42.0 m^2 g^{-1}), $CeAlNi_4$ (66.9 m^2 g^{-1}), and $Sm(NiSi)_2$ (25.0 m^2 g^{-1}) were subsequently evaluated for their catalytic activity in the $NaBH_4$-assisted hydrogenation process of 4-nitrophenol. In comparison with the widely used Ni/CeO_2 catalyst, both $ZrZnNi_4$ and $Sm(NiSi)_2$ exhibited superior catalytic performance. Given that the WFs of Zr and Sm are considerably lower than that of Ni, which serves as the active site for hydrogenation, it was hypothesized that this high catalytic performance arises from the generation of electron-rich Ni species, particularly in the case of $ZrZnNi_4$.

Author contributions

Yasukazu Kobayashi: conceptualization, supervision, funding acquisition, investigation, methodology, data curation, writing – original draft, writing – review & editing. Hiroshi Mizoguchi: investigation, methodology, data curation, writing – review & editing. Koharu Yamamoto: investigation, methodology, data curation, writing – review & editing. Ryo Shoji: methodology, writing – review & editing.

Conflicts of interest

There are no conflicts to declare.

Data availability

The authors declare that the data supporting the findings of this study are available within the paper and its supplementary information (SI). Supplementary information is available. See DOI: https://doi.org/10.1039/d6dt00513f.

Should any raw data files be needed in another format they are available from the corresponding author, Yasukazu Kobayashi, upon reasonable request.

Acknowledgements

This work was supported by JSPS KAKENHI Grant Numbers 24K08591 and 23K23440. A part of this work was supported by "Advanced Research Infrastructure for Materials and Nanotechnology in Japan (ARIM)" of the Ministry of Education, Culture, Sports, Science and Technology (MEXT). Proposal Number JPMXP125NM5175. We acknowledge Mr Koei Takagi for his help in review process.

References

1 Z. Xiong, H. Zhang, W. Zhang, B. Lai and G. Yao, *Chem. Eng. J.*, 2019, **359**, 13–31.
2 P. K. Arora, A. Srivastava and V. P. Singh, *J. Hazard. Mater.*, 2014, **266**, 42–59.
3 T. Aditya, A. Pal and T. Pal, *Chem. Commun.*, 2015, **51**, 9410–9431.
4 S. Wunder, F. Polzer, Y. Lu, Y. Mei and M. Ballauff, *J. Phys. Chem. C*, 2010, **114**, 8814–8820.
5 R. Retnamma, A. Q. Novais and C. M. Rangel, *Int. J. Hydrogen Energy*, 2011, **36**, 9772–9790.
6 J. Strachan, C. Barnett, A. F. Masters and T. Maschmeyer, *ACS Catal.*, 2010, **10**, 5516–5521.
7 M. I. Din, R. Khalid, Z. Hussain, T. Hussain, A. Mujahid, J. Najeeb and F. Izhar, *Crit. Rev. Anal. Chem.*, 2020, **50**, 322–338.
8 K. Zhang, J. M. Suh, J.-W. Choi, H. W. Jang, M. Shokouhimehr and R. S. Varma, *ACS Omega*, 2019, **4**(1), 483–495.
9 P. Zhao, X. Feng, D. Huang, G. Yang and D. Astruc, *Coord. Chem. Rev.*, 2015, **287**, 114–136.
10 T. R. Mandlimath and B. Gopal, *J. Mol. Catal. A:Chem.*, 2011, **350**, 9–15.
11 M. S. Qatan, F. Arshad, M. Miskam and G. A. Naikoo, *Int. J. Environ. Sci. Technol.*, 2024, **21**, 5247–5268.
12 H. B. Michaelson, *J. Appl. Phys.*, 1977, **48**, 4729–4733.
13 Y. Kobayashi, S. Tada and R. Kikuchi, *Mater. Trans.*, 2020, **61**, 1037–1040.
14 J. P. Perdew, K. Burke and M. Ernzerhof, *Phys. Rev. Lett.*, 1996, **77**, 3865.
15 P. E. Blöchl, *Phys. Rev. B: Condens. Matter Mater. Phys.*, 1994, **50**, 17953.
16 G. Kresse and J. Furthmüller, *Phys. Rev. B: Condens. Matter Mater. Phys.*, 1996, **54**, 11169.
17 E. Sanville, S. Kenny, R. Smith and G. Henkelman, *J. Comput. Chem.*, 2007, **28**, 899–908.
18 K. Momma and F. Izumi, *J. Appl. Crystallogr.*, 2011, **44**, 1272–1276.
19 F. Pourarian and W. E. Wallace, *J. Less-Common Met.*, 1982, **87**, 275–281.
20 V. Babizhetskyy, O. Myakush, A. Simon and B. Kotur, *Intermetallics*, 2013, **38**, 44–48.
21 E. Parthe, *Z. Kristallogr. – Cryst. Mater.*, 2006, **221**, 301–304.
22 Z. Blazina, A. Drasner and Z. Ban, *J. Nucl. Mater.*, 1981, **96**, 141–146.
23 A. L. Allred and E. G. Rochow, *J. Inorg. Nucl. Chem.*, 1958, **5**, 264–268.
24 H. Mizoguchi, S. W. Park and H. Hosono, *J. Am. Chem. Soc.*, 2021, **143**, 11345–11348.
25 H. Nesbitt, D. Legrand and G. Bancroft, *Phys. Chem. Miner.*, 2000, **27**, 357–366.
26 C. Morant, J. M. Sanz, L. Galán, L. Soriano and F. Rueda, *Surf. Sci.*, 1989, **218**, 331–345.
27 M. C. Biesinger, L. W. M. Lau, A. R. Gerson and R. S. C. Smart, *Appl. Surf. Sci.*, 2010, **257**, 887–898.
28 E. Bêche, P. Charvin, D. Perarnau, S. Abanades and G. Flamant, *Surf. Interface Anal.*, 2007, **40**, 264–267.
29 P. M. A. Sherwood, *Surf. Sci. Spectra*, 1998, **5**, 1–3.
30 C. Chen, S. J. Splinter, T. Do and N. S. McIntyre, *Surf. Sci.*, 1997, **382**, L652–L657.
31 J. Zhu, Y. Ma and S. Zhuang, *Surf. Sci.*, 2009, **603**, 1802–1811.
32 R. Alfonsetti, L. Lozzi, M. Passacantando, P. Picozzi and S. Santucci, *Appl. Surf. Sci.*, 1993, **70–71**, 222–225.
33 Y. Kobayashi, K. Yamamoto and R. Shoji, *Crystals*, 2024, **14**(3), 278.
34 Y. Kobayashi, S. Yokoyama and R. Shoji, *Metals*, 2024, **14**(4), 443.
35 Y. Kobayashi, H. Y. Teah, S. Yokoyama, R. Shoji and N. Hanada, *ACS Sustainable Chem. Eng.*, 2022, **10**(46), 15046–15057.
36 Y. Kobayashi, H. Y. Teah, S. Yokoyama, R. Shoji and N. Hanada, *Int. J. Hydrogen Energy*, 2023, **48**, 30963–30973.